ARTICLES
https://doi.org/10.1038/s41928-021-00556-2
nature electronics

Check for updates

An on-skin platform for wireless monitoring of flow rate, cumulative loss and temperature of sweat in real time

Kyeongha Kwon[1,2,15], Jong Uk Kim[2,3,15], Yujun Deng[4,5,15], Siddharth R. Krishnan[2,6], Jungil Choi[7], Hokyung Jang[2,8], KunHyuck Lee[9], Chun-Ju Su[2], Injae Yoo[1], Yixin Wu[9], Lindsay Lipschultz[10], Jae-Hwan Kim[11], Ted S. Chung[10], Derek Wu[2,12], Yoonseok Park[2], Tae-il Kim[3,13], Roozbeh Ghaffari[2,10], Stephen Lee[2], Yonggang Huang[2,5,9,12] and John A. Rogers[2,9,10,12,14] ✉

Monitoring the flow rate, cumulative loss and temperature of sweat can provide valuable physiological insights for the diagnosis of thermoregulatory disorders and illnesses related to heat stress. However, obtaining accurate, continuous estimates of these parameters with high temporal resolution remains challenging. Here, we report a platform that can wirelessly measure sweat rate, sweat loss and skin temperature in real time. The approach combines a short, straight fluid passage to capture sweat as it emerges from the skin with a flow sensor that is based on a thermal actuator and precision thermistors, and that is physically isolated from, but thermally coupled to, the sweat. The platform transfers data autonomously using a Bluetooth Low Energy system on a chip. Our approach can also be integrated with advanced microfluidic systems and colorimetric chemical reagents for the measurement of pH and the concentration of chloride, creatinine and glucose in sweat.

Sweat rate is an important health marker that provides information about hydration state, stress and physical exertion[1–3]. The resulting insights can be used to develop optimized strategies for fluid intake[4–7]. Sweat rates are typically measured using the whole-body wash method[8], which requires strictly controlled laboratory conditions. Alternatively, absorbent pads can yield regional sweat rates[9,10], but they also require laboratory-based analysis and do not provide real-time information. Skin-interfaced device platforms have recently been developed that exploit optical and/or electrochemical methods and can monitor sweat loss and sweat chemistry[11–13] by means of individualized, real-time measurements[14,15]. Microfluidic systems that use lab-on-a-chip technologies and colour-responsive chemistries are particularly powerful because of their ability to provide visual readout of a range of key information related to sweat[16,17]. Nevertheless, for certain applications (including worker safety, military training and contact sports), protective equipment limits visual inspection of such devices.

Emerging techniques, such as wearable conductivity sensors[18], enable real-time monitoring of sweat rate, but they rely on contact of the electrodes with sweat, which can be affected by salt build-up in the chamber, contamination and corrosion, as well as other detrimental phenomena. Systems that use calorimetric sensing for determining sweat rates have also been developed[19,20], but they also require direct electrical interfaces to the sweat, as well as high levels of power consumption (~80 mA at 5 V (ref. [19]) and 3.3 V (ref. [20])). Such approaches demand careful cleaning and sterilization between cycles of use, and they require large batteries, which limits their re-use and comfort.

In this Article, we report a skin-interfaced platform that can wirelessly monitor the flow rate, cumulative loss and temperature of sweat in real time. The platform captures sweat as it emerges from the surface of the skin, using a short, straight fluid passage. The method thus avoids the need for complex microfluidic networks and it isolates the electronics from the surrounding biofluids. The platform uses a non-invasive flow sensor consisting of a power-efficient thermal actuator and a collection of precision thermistors, all thermally coupled to the sweat but not in direct contact with it. The approach can measure and wirelessly transmit sweat rates across the physiologically relevant range (from 0 to 5 μl min^{-1})[16] in a manner that minimizes sensitivity to environmental fluctuations (air currents/convection) and changes in body temperature over a practical span (such as 25 °C to 35 °C). For automatic and continuous (up to 200-Hz sampling rate) updates to user-friendly portable devices, we integrate a Bluetooth Low Energy (BLE) system-on-a-chip (SoC) wireless platform that combines Wheatstone-bridge circuits with reference thermistors and variable gain amplifiers (VGAs).

[1]School of Electrical Engineering, Korea Advanced Institute of Science and Technology, Daejeon, Republic of Korea. [2]Querrey-Simpson Institute for Bioelectronics, Northwestern University, Evanston, IL, USA. [3]School of Chemical Engineering, Sungkyunkwan University, Suwon, Gyeonggi-do, Republic of Korea. [4]State Key Laboratory of Mechanical System and Vibration, Shanghai Jiao Tong University, Shanghai, China. [5]Department of Civil and Environmental Engineering, Northwestern University, Evanston, IL, USA. [6]Department of Materials Science and Engineering, University of Illinois at Urbana-Champaign, Urbana, IL, USA. [7]School of Mechanical Engineering, Kookmin University, Seoul, Republic of Korea. [8]Department of Electrical & Computer Engineering, University of Wisconsin, Madison, WI, USA. [9]Department of Materials Science and Engineering, Northwestern University, Evanston, IL, USA. [10]Department of Biomedical Engineering, Northwestern University, Evanston, IL, USA. [11]Department of Electrical and Computer Engineering, University of Illinois at Urbana-Champaign, Champaign, IL, USA. [12]Department of Mechanical Engineering, Northwestern University, Evanston, IL, USA. [13]Department of Biomedical Engineering, and Biomedical Institute for Convergence, Sungkyunkwan University, Suwon, Gyeonggi-do, Republic of Korea. [14]Departments of Neurological Surgery, Chemistry, Electrical Engineering and Computer Science, Northwestern University, Evanston, IL, USA. [15]These authors contributed equally: Kyeongha Kwon, Jong Uk Kim, Yujun Deng. ✉e-mail: jrogers@northwestern.edu

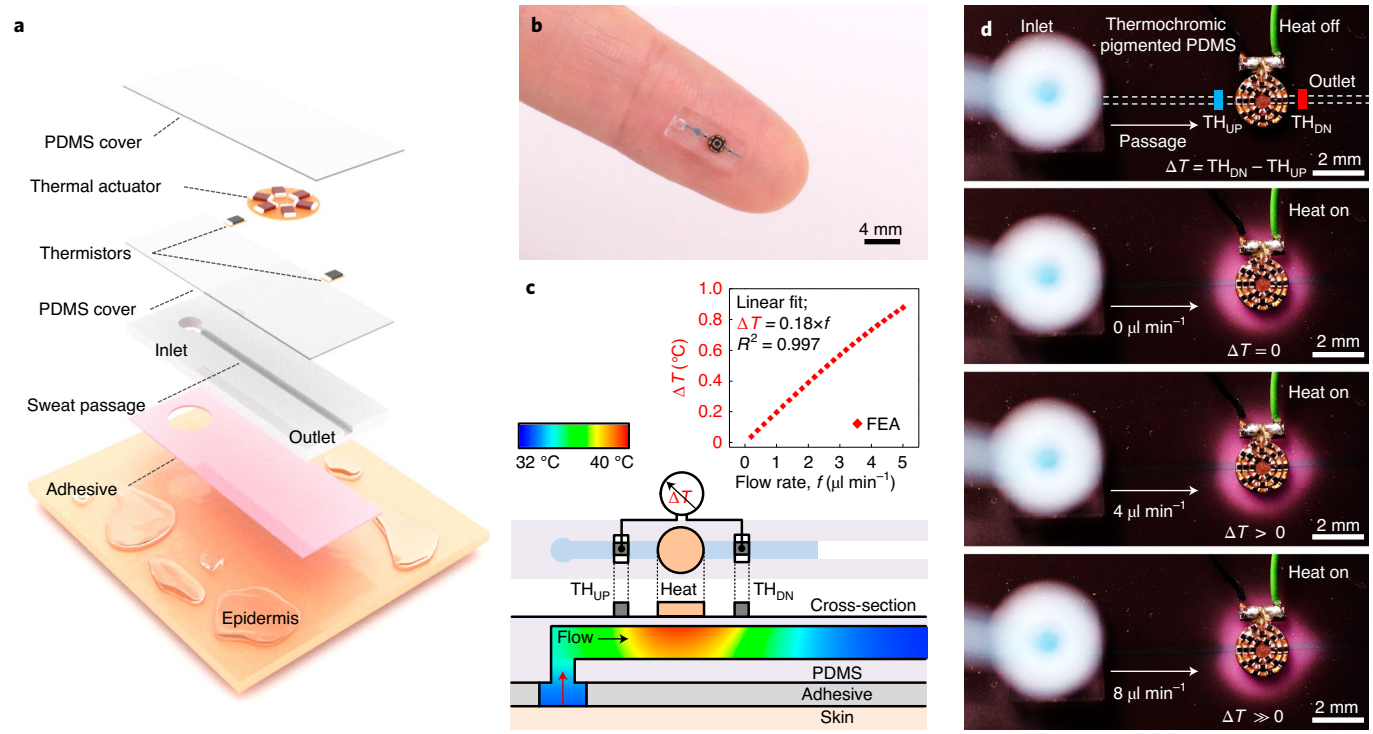

Fig. 1 | Design features and operating principles of a miniaturized, flexible module for remote, on-skin sensing of sweat rate. a, Exploded-view illustration of the module and its interface with the skin. A straight passage (length > 3.4 mm) moulded into a structure of PDMS interfaces to the skin through an inlet opening to allow entry of sweat as it emerges from the surface of the skin. A thermal actuator and two thermistors are mounted on the outer top surface of this passage to support measurements of flow rate by thermal processes, without physical contact with the sweat. **b**, Photograph of a thermal flow sensing module on an index finger. **c**, FEA of the distribution of temperature through the passage filled with sweat flowing at a rate of 4 μl min^{-1}. The sweat transfers heat from the thermal actuator to a downstream thermistor, thereby increasing its temperature relative to that of an upstream thermistor located at an identical distance from the thermal actuator in the upstream direction (TH_{DN} and TH_{UP}). The inset shows FEA results that connect the temperature difference ($\Delta T = TH_{DN} - TH_{UP}$) to the flow rate ($f$) with a simple, linear empirical relationship, $\Delta T = 0.18 \times f$ ($R^2 = 0.997$). **d**, Images of a thermal actuator on a fluid passage formed with PDMS doped with a thermochromic dye that changes its colour from black to pink at temperatures above 25 °C. Flow in the passage transfers heat (pink region) in the downstream direction. From top to bottom: heat off; heat on, flow at 0 μl min^{-1}; heat on, flow at 4 μl min^{-1}; heat on, flow at 8 μl min^{-1}.

In contrast to other systems[16–18], the active components remain separated from the body and the sweat, and operation does not impose limits on the measurable volumes of sweat. On-body measurements across different body locations, at different body temperatures and during exercise and while at rest, demonstrate the key capabilities. The system can also be integrated with advanced microfluidic systems for colorimetric detection of pH as well as the concentrations of chloride, glucose and creatinine.

Non-invasive, miniaturized flow sensors

The sensor incorporates a thermal actuator with two thermistors (Fig. 1a) that measure the temperature upstream and downstream relative to the flow direction. These components are laminated on top of a thin, elastomeric structure that interfaces with an opening (inlet) where sweat enters the system from the surface of the skin before passing under the sensor to a corresponding outlet. A double-sided, skin-safe adhesive with a hole (of radius r) aligned to the inlet provides a robust, water-tight seal and determines the sweat collection area (πr^2). As in the design highlighted in Fig. 1b, the actuator (diameter of 2 mm) consists of eight resistors ($8 \times 35.6\,\Omega$) in series. Applied current generates a constant thermal power density ($P_d = 9.07$ mW mm^{-2}) at the top surface of the structure and, by thermal diffusion, delivers heat to the flowing sweat below (width, height and top layer thicknesses of 500 μm, 125 μm and 70 μm, respectively). The flow transports heat from the actuator directionally downstream, thereby creating a difference between the temperature at the locations of the downstream (TH_{DN}) and upstream (TH_{UP}) thermistors. For the device reported here, the thermistors (width and length of 0.3 mm and 0.6 mm, respectively) lie at positions 1.7 mm downstream and upstream from the centre of the actuator. The results of computational modelling connect the temperature difference ΔT to the flow rate f, given the geometrical features of the system and the constitutive properties of the materials. Figure 1c shows computational predictions for the temperature distribution for flow at a rate of 4 μl min^{-1}, which is representative for sweating on the forearm for male participants riding a stationary bike. The inset presents the results of finite-element analysis (FEA), which establishes a simple, linear empirical relationship, $\Delta T = 0.18 \times f$, with $R^2 = 0.997$, that is applicable across the full range of physiologically relevant rates of sweating during exercise for the particular system described here (see Supplementary Note 1 for details).

To illustrate and visualize the thermal physics, Fig. 1d shows images of a test structure formed in poly(dimethylsiloxane) (PDMS) mixed with a thermochromic powder that changes colour from black to pink at temperatures above 25 °C, for the cases of heat off/flow at 0 μl min^{-1} and heat on/flow at 0, 4 and 8 μl min^{-1} (from top to bottom). Here, the continuous flow of water from an inlet on the left (white circle) through a fluid passage (dashed lines) to the right introduces a corresponding skew in the shape of the pink region. The geometry of the thermal actuator and sensors, along with the dimensions of the passage and the thermal properties of the

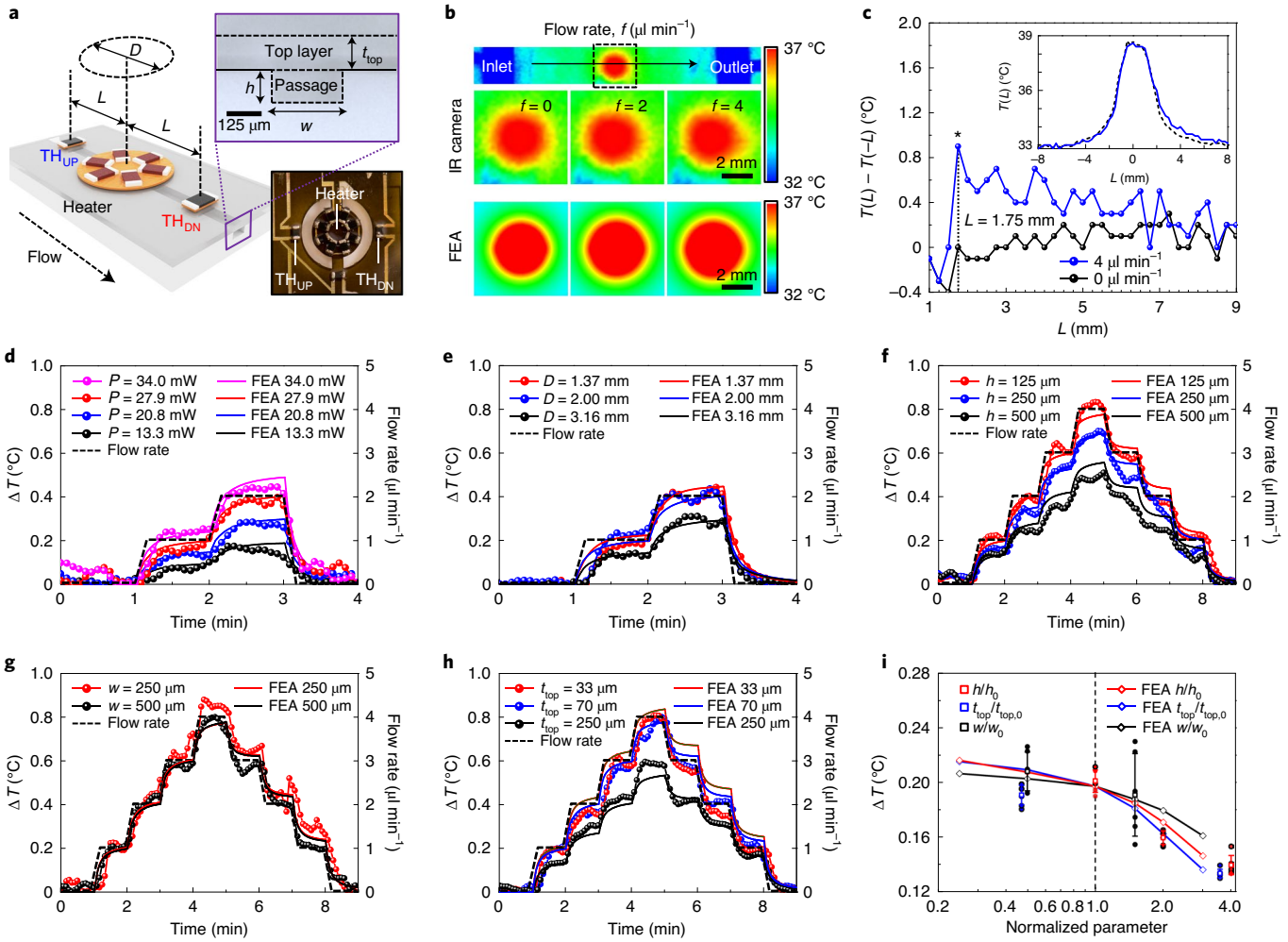

Fig. 2 | Experimental studies and FEA of key characteristics of the thermal flow sensor. a, Schematic of the geometry of a thermal actuator with upstream and downstream thermistors TH_{UP} and TH_{DN} resting on the top outer surface of a fluid passage with design parameters for benchtop studies and FEA: diameter of the thermal actuator (D), distance between the actuator and a thermistor (L), width (w) and height (h) of the passage, and thickness of the top layer (t_{top}). **b**, Infrared images and FEA results for the temperature distribution of an actuator mounted on a passage placed on a hot plate with surface temperature of 34 °C. **c**, Linear temperature profile (inset) within the passage as a function of the distance from the actuator, for flow of 0 and 4 μl min^{-1}, and the temperature difference, $T(L) - T(-L)$, which reaches a maximum for $L = 1.75$ mm. **d**–**h**, The temperature difference (ΔT) measured (symbols) and determined by FEA (line) between the thermistors for different design parameters: the electrical power (P) consumed by the heater (**d**), D (**e**), h (**f**), w (**g**) and t_{top} (**h**). **i**, Measurement (square data points) and FEA (diamonds and rules) results for ΔT for a constant flow of 1 μl min^{-1} as a function of normalized design parameters: h/h_0, w/w_0, $t_{top}/t_{top,0}$ where h_0, w_0 and $t_{top,0}$ denote 125 μm, 500 μm and 70 μm, respectively. Data are presented as mean values (squares) ± s.d. (vertical error bars) measured over a 1-min averaging window (sample size = 6).

constituent materials, all affect the sensitivity of the measurement, as defined in detail in the following section.

Thermal physics associated with the flow sensors

Benchtop studies (for details see Methods and Supplementary Fig. 1) and computational predictions serve to validate the models of thermal transport and to allow for optimized selection of the design parameters. The heat transfer characteristics depend mainly on certain design parameters: the distance L between the centre of the thermal actuator and thermistors TH_{UP} and TH_{DN}, the thermal actuation power P, the diameter of the actuator D and the height h, width w and thickness of the top layer (t_{top}) of the passage (Fig. 2a). The insets in Fig. 2a show a cross-sectional microscope image of a passage (top) and an image of a heater and radially equidistant thermistors (bottom). Figure 2b presents infrared images (top) and FEA results (bottom) of anisotropic temperature distributions aligned to the direction of flow at rates (f) of 0, 2 and 4 μl min^{-1} (from left to right). Here, the thermal actuator ($D = 2$ mm, $P = 28$ mW) and associated thermistors are mounted on the surface of a structure ($w \times h = 500\,\mu m \times 125\,\mu m$, $t_{top} = 70\,\mu m$) that rests on a hot plate at a surface temperature (T_s) of 34 °C, comparable to that of skin under ambient conditions. The infrared camera (FLIR Systems, a6255sc) captures the temperature profiles, $T(L)$, across the heater located at $L = 0$, where L ranges from −6 mm to 6 mm along the direction of flow (Fig. 2c). The profile (inset) is symmetrical with respect to the heater located at $L = 0$ for $f = 0$ μl min^{-1} (black dashed line) and skews toward the downstream direction ($+L$ direction) at $f = 4$ μl min^{-1} (blue line). The temperature difference, $T(L) - T(-L) = \Delta T$, for L ranging from 1.00 to 9.00 mm (with increments of 0.25 mm) has a small value (~0.0 °C) for $f = 0$ μl min^{-1} and reaches a maximum (~0.9 °C) at $L = 1.75$ mm for $f = 4$ μl min^{-1}. The values of ΔT determined by FEA for $f = 0$, 1, 2, 3 and 4 μl min^{-1} at five different L values of 1.4, 1.7, 2.0, 3.0 and 3.5 mm are provided in Supplementary Fig. 2. Increasing the thermal actuation power

(P) or the power density ($P_d = P/\pi D^2$) increases ΔT for a constant flow rate ($\Delta T/f$), but also increases the current consumption and therefore decreases the battery life. For $L = 1.75$ mm, Fig. 2d,e shows wireless measurements (symbols) and FEA results (lines) for ΔT, for $P = 13.3$, 20.8, 27.9 and 34.0 mW (Fig. 2d) and $D = 1.37$, 2.00 and 3.16 mm (Fig. 2e), respectively. The black dashed lines show changes in flow rate. The value of $\Delta T/f$ increases with increasing P or P_d, and the values of $\Delta T/f/P$ (with $f = 1$ and 2 μl min^{-1} and $P = 13.3$, 20.8, 27.9 and 34.0 mW) are constant at 7.1 ± 0.1 °C (μl min^{-1})$^{-1}$ W^{-1} (FEA results) and 6.8 ± 0.8 °C (μl min^{-1})$^{-1}$ W^{-1} (wireless measurements). Selection of $P = 27.9$ mW and $D = 2.00$ mm yields a sensitivity of 0.2 °C (μl min^{-1})$^{-1}$ with a top surface temperature of the thermal actuator that remains less than 40 °C (Fig. 2c). The data in Fig. 2f–h correspond to wireless measurements and FEA results for the time dependence of ΔT for changes in flow rate with different design parameters of the fluid passage: h (Fig. 2f; $w = 500$ μm, $t_{top} = 70$ μm), w (Fig. 2g; $h = 125$ μm, $t_{top} = 70$ μm) and t_{top} (Fig. 2h; $w \times h = 500$ μm × 125 μm). Figure 2i presents the measurements and FEA results for ΔT for a constant flow of 1 μl min^{-1} as a function of normalized design parameters: h/h_0, w/w_0, $t_{top}/t_{top,0}$, where h_0, w_0 and $t_{top,0}$ are 125 μm, 500 μm and 70 μm, respectively. Decreasing h or t_{top} corresponds to increasing the flow velocity, v = flow (f)/cross-sectional area of the fluid passage ($w \times h$) for a given f, or the heat flux between the heating elements/sensors and the flowing fluid, respectively. The result increases ΔT for a constant flow of $f = 1$ μl min^{-1}. Because decreasing w increases the flow velocity but decreases the heat flux, this parameter has a relatively small effect on sensitivity.

Additional studies focus on the reliability of the measurement under various conditions relevant to practical use—that is, different temperature conditions, levels of airflow and mechanical vibrations, and use over extended periods (1 h) during gradual changes in flow ranging from 0 to 2 μl min^{-1} (for details see Supplementary Note 2 and Supplementary Figs. 3–5). The results indicate stable operation across 10 °C changes in temperature, airflow rates of 1.5 m s^{-1} from the top, mechanical oscillations at 5 Hz with an amplitude of 2 mm, and for 1 h of testing.

Variables that influence the temperature difference (ΔT), in addition to the sweat flow rate f, include thermal conductivity k, heat capacity c, and density ρ of the fluid (subscript 'F') and the solid PDMS passage (subscript 'p'), as well as the geometric parameters of the device (w, h, t_{top}, D and L) and the power density of the actuator (P_d) (Supplementary Fig. 6 and Supplementary Table 3). Combining steady-state heat transfer equations and FEA (for details see Supplementary Note 3 and Supplementary Figs. 7 and 8), a linear analytical scaling law can be obtained between the normalized temperature difference $\frac{k_F \Delta T}{L P_d}$ and the normalized flow rate $\frac{f \rho_F C_F}{D k_F}$ as

$$\frac{k_F \Delta T}{L P_d} = \frac{f \rho_F c_F}{D k_F} g\left(\frac{L}{D}, \frac{t_{top}}{h}, \frac{k_p}{k_F}\right)$$

The function in this scaling law depends on only two non-dimensional geometric parameters and one non-dimensional thermal property: L/D and t_{top}/h represent the effect of heat transfer along the flow direction and the depth direction, respectively, and k_p/k_F represents the effect of thermal conductivity. Reducing L/D, t_{top}/h and k_p/k_F can increase the device sensitivity, which is shown as the slope of the normalized temperature difference with respect to the normalized flow rate (Supplementary Fig. 9).

Circuit designs and operating principles

The device in Fig. 3a is a wireless, non-invasive, reusable system for continuous, real-time measurements of the flow of sweat between an inlet and outlet, in a platform designed for real-world use and without any direct contact with sweat, based on considerations from thermal physics and engineering design, as highlighted in the previous section. The width, length, height and weight of the device, excluding the button cell battery (MS621FE), are 11.2 mm, 24.8 mm, 1.2 mm and 203.0 mg, respectively. The inset presents a side view. The wireless platform consists of a thermal flow-sensing module (TFM) and a BLE SoC for control and wireless communication (Fig. 3b). A key feature of the TFM is that it uses a reference thermistor as one leg of a Wheatstone-bridge circuit, followed by differential amplifiers cascaded by VGAs, with gain automatically controlled by the central processing unit (CPU) of the BLE SoC depending on the temperature measurements. The reference thermistor (TH_{REF}) resides outside the fluid passage but at the same distance from the thermal actuator as TH_{UP} and TH_{DN}. The changes in environmental temperature affect this TH_{REF} in the same manner as the other thermistors, thereby naturally eliminating the effects of these changes (for example, due to variations in the skin and/or the surrounding air). A VGA, subsequent to the Wheatstone-bridge circuit, amplifies the voltage outputs from the bridge, with an adaptive gain (for example, from 1/6 to 4) to maximize the accuracy of the measurements of resistance (for example, from 0.22 Ω to 0.01 Ω) within the required dynamic range.

Figure 3b presents circuit and block diagrams of the TFM and BLE SoC for wireless communication to an external user interface (smartphone). A software toggle switch enables a BLE connection to the device and activates a general-purpose input/output pin to source a predetermined current (~10 mA) into the resistive heater. As described above, the TFM consists of a thermal actuator (Joule heating through 8 × 35.6 Ω resistors), Wheatstone-bridge circuits include the three thermistors (TH_{UP}, TH_{DN} and TH_{REF}) with a known resistor (R) on each bridge, and two differential amplifiers (AMPs). Each AMP amplifies the differences between the voltages on TH_{UP} and TH_{DN} and the voltage on TH_{REF} to eliminate the effects of temperature differences due to environmental changes, as mentioned previously. The subsequent variable gain amplifiers (VGAs) buffer the outputs of the AMPs to the following analogue-to-digital converters (ADCs). The three-channel ADCs monitor the bridge voltages (upstream (V_{UP}), downstream (V_{DN}) and reference (V_{REF}) values) and control the gain of the VGAs before each ADC to achieve the highest resolution within the input voltage range. A central processing unit (CPU) executes digital signal processing on the ADC-sampled data (V_{UP}, V_{DN} and V_{REF}) to filter out noise. Wireless transmission occurs over the BLE radio to the user interface, where algorithms convert the voltages into corresponding temperature values.

Figure 3c provides an exploded-view illustration of the constituent layers and components: silicone encapsulation layers, the Li-polymer battery, mini-magnets, insulation foam electronics, a PDMS structure to define separated inlets and outlets, and adhesives. The electronics uses thin, flexible circuit traces that interconnect the BLE SoC, amplifiers, bridge resistors, thermistors and thermal actuator. Figure 3d shows photographs of an encapsulated device adhered to the skin with and without an encapsulated battery mounted mechanically and electrically via matching magnets.

On-body measurements

A key feature of this platform is that its operation does not rely on an elaborate microfluidic structure, but only on a short, straight flow segment between an inlet interface to the skin and an outlet to the surroundings. A photograph of a device with this simple design is presented in Fig. 4a, where it is shown mounted on the forearm but with an extended configuration that also includes a serpentine microfluidic channel to allow for manual readout of sweat rate and volume as the basis for validating the flow measurements. A water-soluble dye (blue) located at the inlet of this serpentine channel imparts colour to the incoming sweat, thereby producing an easily identifiable filling front. Our studies of the wireless and

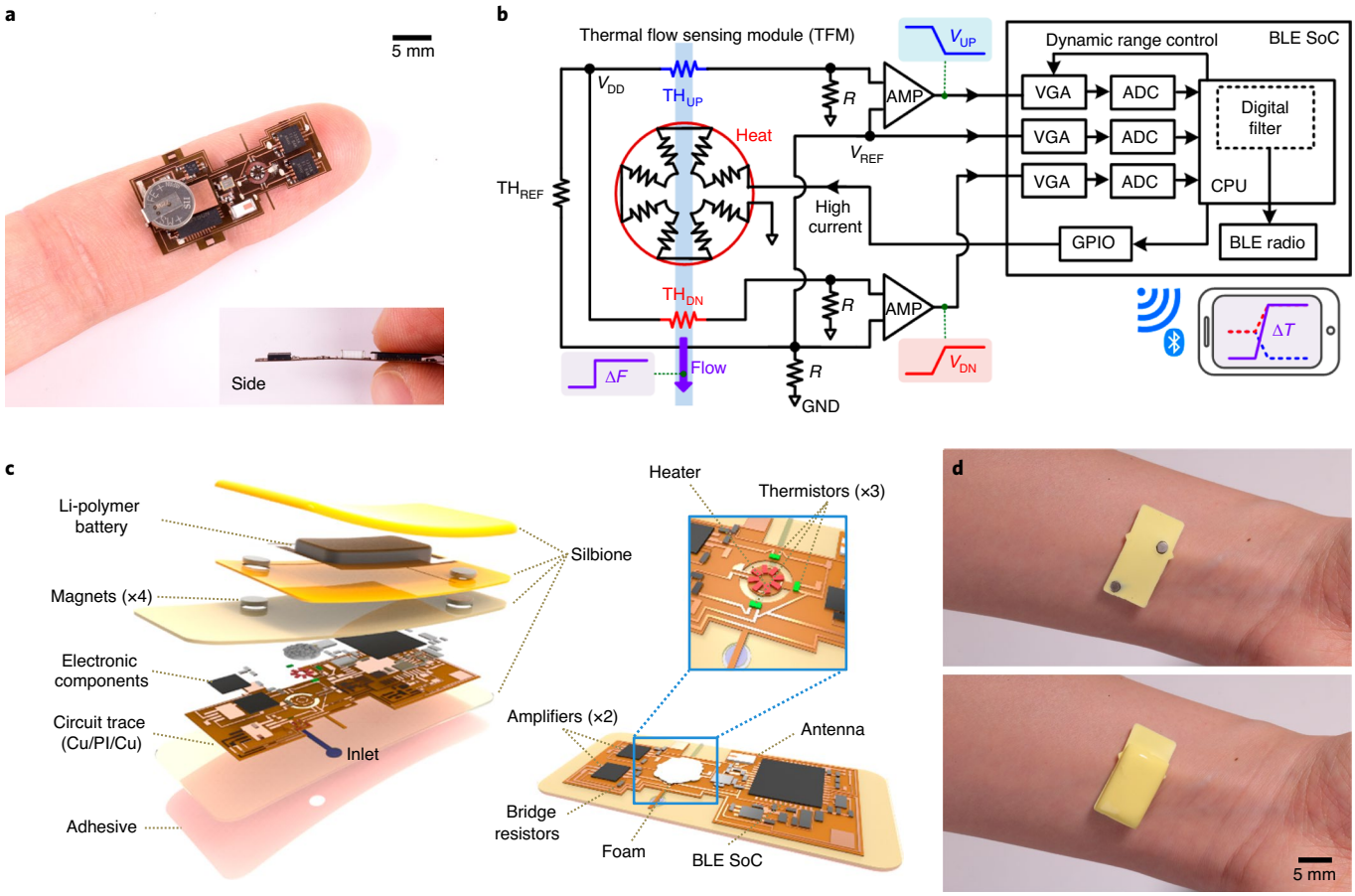

Fig. 3 | A skin-interfaced, wireless system for continuous monitoring of sweat rate, sweat loss and temperature. a, Photograph of a thin, flexible, remote flow-sensing module with BLE communication capabilities, resting on the tip of an index finger. The width (*w*) and length (*l*) of the device are 11.2 mm and 24.8 mm, respectively. The inset provides a side view. **b**, Circuit and block diagrams of the platform and its wireless interface to a smartphone (BLE radio). The flow-sensing module consists of a thermal actuator (Joule heater), Wheatstone-bridge circuits including thermistors (upstream, downstream and reference; TH_{UP}, TH_{DN} and TH_{REF}) with a known resistor (*R*) on each bridge, and two differential amplifiers (AMPs) followed by VGAs. A software toggle switch on the user interface enables BLE connections to the device and activates a general-purpose input/output (GPIO) pin to source a predetermined current into the thermal actuator. A CPU controls digital signal processing on the ADC-sampled data (the bridge voltage, upstream, downstream and reference; V_{UP}, V_{DN} and V_{REF}) and wirelessly transmits the data over the BLE radio to a user interface. **c**, Schematic and exploded-view illustration of the constituent layers: silicone encapsulation layers, an insulation foam (Flex Foam), electronics, fluid passage and adhesives. The electronics includes a BLE SoC, instrumentation amplifiers (×2), bridge resistors (×3), thermistors (×3) and a heater. **d**, Photographs of an encapsulated device on the inner wrist, without a battery (top) and with a magnetically coupled battery (bottom).

manual measurements of sweat rate involved the deployment of devices on the forearms of two healthy volunteers (Fig. 4b): the right forearm for participant 1 and both forearms for participant 2. The system performs temperature measurements at a sampling rate of 200 Hz and transmits an averaged value every 0.1 s (10 Hz) to a user interface. Software applications save the wireless readings (10 data per second) into the memory of the smartphone and display the averaged value every minute, synchronized with manual reading of the position of the filling front by capture and analysis of digital images of the device (right, Fig. 4b). Calibration involves a constant flow of liquid (deionized water) established with a syringe pump over a 1-min measurement period. For flow rates (f) of 0, 1, 2, 3 and 4 μl min^{-1}, the temperature differences are 0.03, 0.19, 0.40, 0.59 and 0.81 °C, respectively (Fig. 4c). As f increases, ΔT increases proportionally such that the calibration factor C of the measured ΔT over f is $C_{meas} = \Delta T/f = 0.20\,°C\,(\mu l\,min^{-1})^{-1}$ ($R^2 = 0.998$). The results of FEA (diamond-shaped markers in Fig. 4c) indicate a calibration factor of $0.18\,°C\,(\mu l\,min^{-1})^{-1}$ ($R^2 = 0.997$) for a range of flow rates ($0\,\mu l\,min^{-1} < f < 4\,\mu l\,min^{-1}$). The wireless measurements (red linear fit line) are in good agreement (~90%) with the FEA results.

Figure 4d–f shows the results of manual readings of f (purple, blue and red symbols, respectively) and wireless measurements of ΔT (black markers) as a function of time (min), from the right forearm of participant 1 (Fig. 4d) and both forearms of participant 2 (Fig. 4e,f), while cycling and at rest. During the session labelled 'Cycle', ΔT and f increase and reach a constant value, and then decrease to values approaching zero during the session labelled 'Rest'. The data exhibit a strong correlation between physical activity and sweat rate. Vertical error bars (grey) on the graphs represent the s.d. of ΔT measured over a 1-min averaging window. Errors in the flow rate, $f_e = f - \Delta T/C_{meas}$, as a function of time are summarized in Supplementary Fig. 10. The results from the right forearm of participant 1 and the left and right forearms of participant 2 have mean values of $f_{e,mean} = 0.04$, −0.40 and −0.16 μl min^{-1}, respectively, with s.d. of $f_{e,s.d.} = 0.48$, 0.33 and 0.36 μl min^{-1}. Figure 4g–i shows plots of cumulative ΔT ($\Sigma\Delta T$, diamonds) and local sweat loss (Σf; squares) as a function of time measured from the forearm of participant 1 (Fig. 4g) and the left (Fig. 4h) and right (Fig. 4i) forearms of participant 2. Manual readings of the collected sweat multiplied by the calibration factor ($C \times \Sigma f$; circles) correspond to the summed

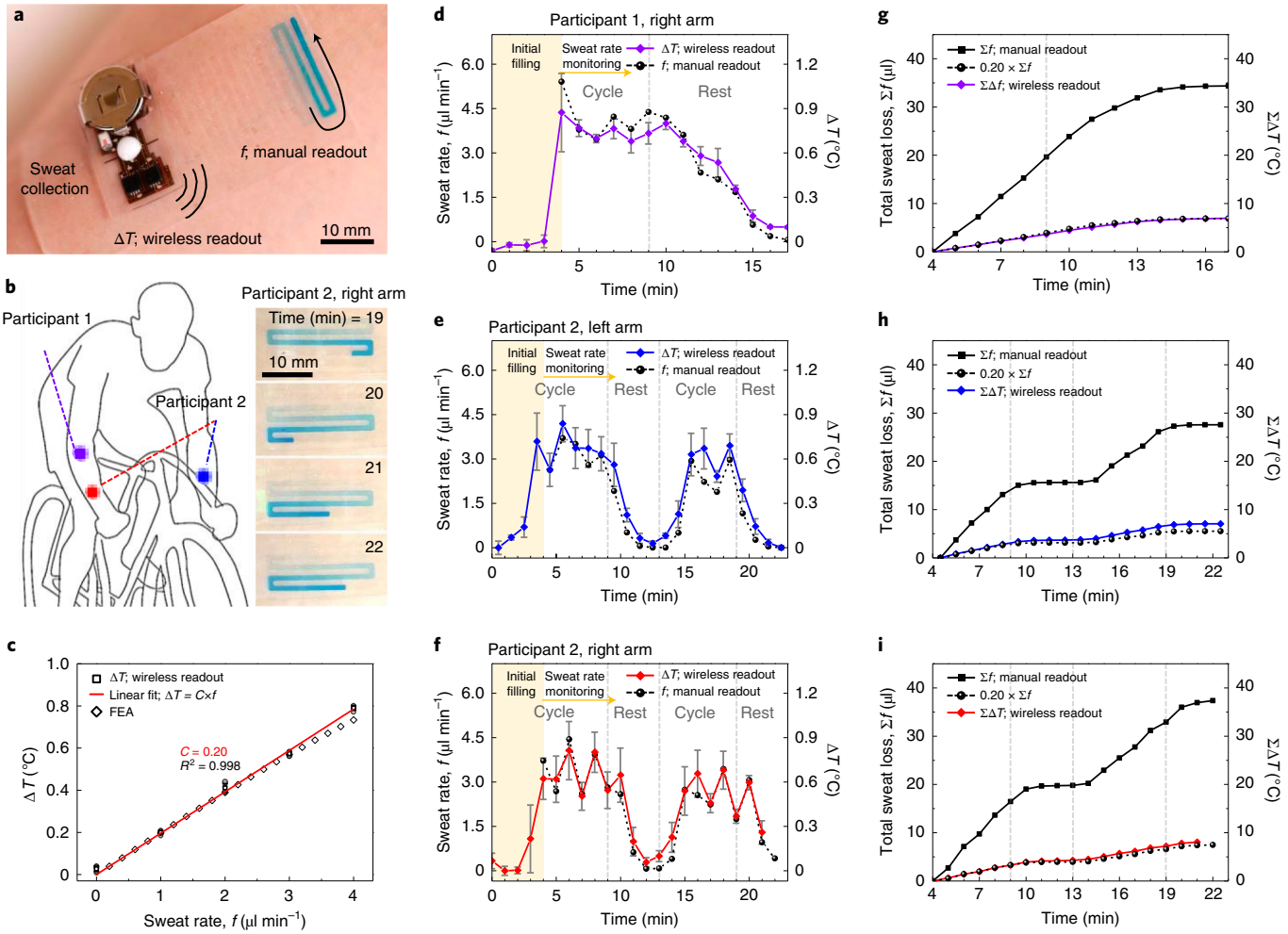

Fig. 4 | On-body measurements of sweat flow rate and total loss for physical activity and dehydration monitoring. a, Photograph of a wireless, skin-interfaced system for continuous, wireless measurement of sweat flow rate, and the microfluidic structure for visual readout, mounted on the forearm. A water-soluble dye (blue) located at the inlet imparts colour to the incoming sweat as it flows past, thereby enabling a visually identifiable filling front in the passage. **b**, Mounting positions (left) on the body (the right forearm for participant 1 and both forearms for participant 2) and images (right) of the filling front in the fluid passage mounted on the right forearm of participant 2. **c**, Wirelessly measured temperature difference (ΔT) as a function of flow rate (f), as well as its linear fit. Data are presented as data points (circles) and mean values ± s.d. (squares and vertical error bars, respectively; sample size = 6). The calibration factor is $C = \Delta T/f = 0.20$ ($R^2 = 0.998$). **d**–**f**, Wireless readout (mean values ± s.d.; sample size = 600) of ΔT every 1 min (purple, blue and red diamonds) and manual readout of the collected sweat rate (f) every 1 min (black circles) during field testing with healthy participants while cycling and at rest: right arm of participant 1 (**d**), and left (**e**) and right (**f**) arms of participant 2. **g**–**i**, Cumulative ΔT ($\Sigma\Delta T$; diamonds) and sweat loss (Σf; squares) as a function of time, measured from the forearm of participant 1 (**g**), and the left (**h**) and right (**i**) forearms of participant 2. The manual readout of the collected sweat multiplied by the calibration factor ($C \times \Sigma f$; circles) corresponds to the cumulative value of wireless measurements of ΔT.

values of wireless measurements of ΔT with an average error of $e = (\Sigma\Delta T/C - \Sigma f)/\Sigma f = 0.13$.

Multifunctional systems

The types of non-contact, digital wireless measurements of sweat flow rates and total sweat loss described in the previous sections can be easily combined with measurements of sweat chemistry using microfluidic platforms and colorimetric reagents and also with assessments of skin temperature using additional components in the electronics module. For the former, demonstrations focusing on concentrations of chloride and glucose in sweat provide indications relevant to cystic fibrosis (in newborns and infants[21]) and diabetes[22], respectively. Sweat creatinine[23–26] also has potential as a screening marker for kidney dysfunction[27]. The pH of sweat is an indicator of metabolic alkalosis, where the pH shows elevated values relative to the normal range (7.35–7.45) due to decreased hydrogen ion concentration and associated increased concentrations of bicarbonate[28,29]. A simple platform that addresses these needs exploits the corresponding colorimetric chemical reagents (pH[30,31], glucose[30], chloride[30] and creatinine[31]) loaded into a skin-interfaced microfluidic system designed to allow reversible integration with the wireless platform introduced in the previous sections. As illustrated in Fig. 5a, the system supports (1) colorimetric analysis of sweat chloride/glucose/creatinine/pH levels, as well as (2) wireless, digital evaluation of sweat rate and volume. The latter quantities are often critically important in interpreting the former, as sweat chemistry is known to depend on sweat rate and total sweat loss[1,4,15,32,33].

Sweat fills the inlet ports of the device and passes through a short fluid passage (width and height of 500 μm and 125 μm, respectively) from inlet a (inset, Fig. 5a) or enters into a series of microscale reservoirs (μ-RVs; volume of 10 μl) from inlets b–e. The μ-RVs from inlets b–e contain chemical or enzymatic assays for colorimetric detection of pH and the concentrations of chloride, creatinine and glucose, respectively. Each μ-RV fills in a sequential manner

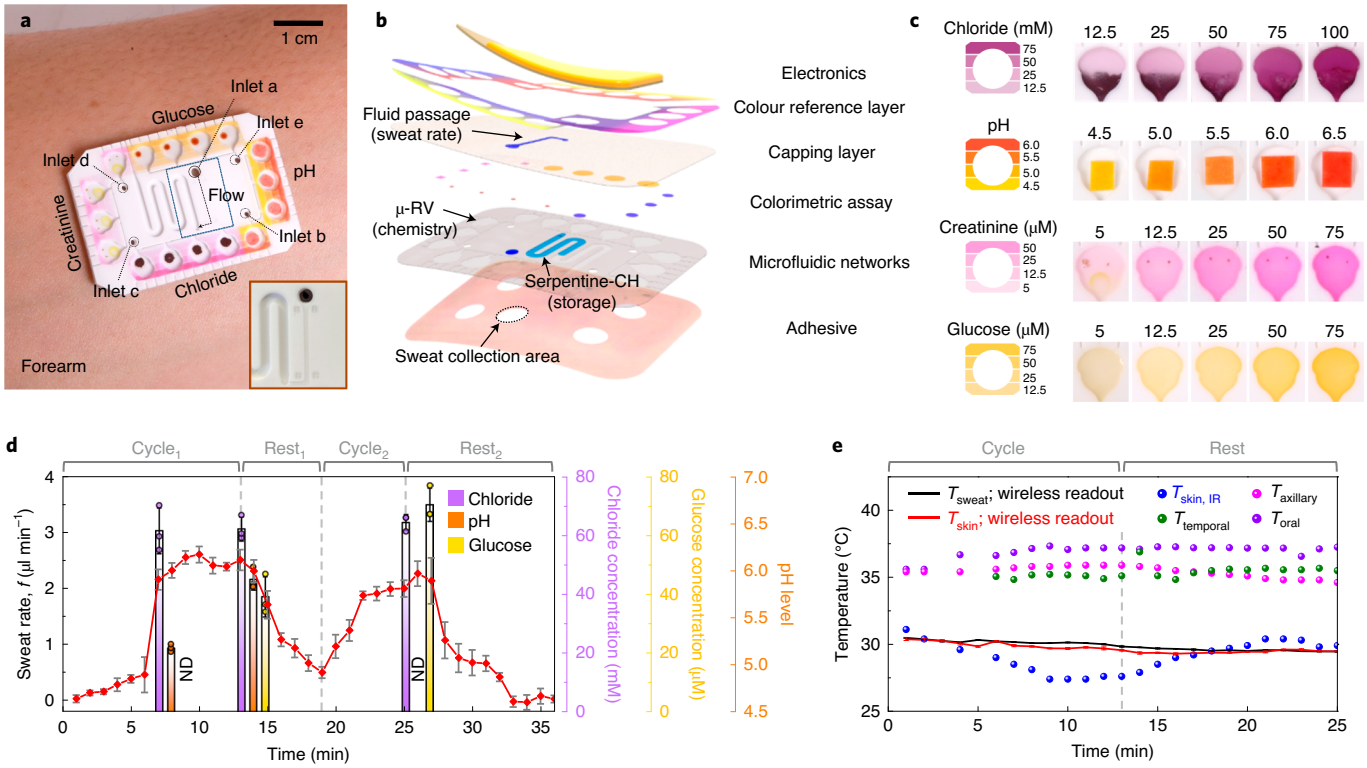

Fig. 5 | Multimodal sensing of sweat rate and loss, skin temperature and various sweat biomarkers. a, Optical image of an advanced skin-interfaced microfluidic system including a short fluid passage for evaluation of sweat rate and loss and microscale reservoirs (μ-RVs) for analysis of the sweat chemistry, with the device mounted on the forearm. Inset: close-up of the short fluid passage connected to the serpentine channel. **b**, Exploded-view illustration of the multilayered structure of the system, comprising a wireless platform, colour reference markers, a capping layer with a fluid passage, colorimetric assays, microfluidic networks and an adhesive layer. **c**, Graphical images of the colour reference markers (left), with colour levels extracted from optical images of the colour development of assay μ-RVs as a function of sample concentrations (right) of chloride, pH, creatinine and glucose (top to bottom). **d**, Multimodal sensing of sweat chloride/glucose/pH levels (purple, yellow, orange, respectively) and rate and loss (red). Data are presented as mean values (bar graph) ± s.d. (vertical error bars, black) and data points (circles) of sweat concentration measured at three different locations from each assay (sample size = 3), and as mean values (diamonds) ± s.d. (vertical error bars, grey) of sweat rate and loss measured over a 1-min averaging window (sample size = 600). Creatinine measurements are not shown because the concentrations were below the detection range. ND represents data not collected due to insufficient sweat generation. **e**, Results of manual readout of oral (T_{oral}, purple), axillary ($T_{axillary}$, pink), temporal ($T_{temporal}$, green) and skin ($T_{skin,IR}$, blue) temperatures using commercial thermometers, and wireless readout of sweat (black) and skin (red) temperatures as a function of time (min) while cycling and at rest.

(from #1 to #4, Supplementary Fig. 11) due to the action of capillary bursting valves (CBVs)[30], thereby allowing for the measurement of changes in the concentrations of these species in sweat as a function of sweat loss. The exploded-view illustration of the system in Fig. 5b highlights the multilayered structure: the reusable wireless platform, the colour reference layer, a capping layer with a short fluid passage, colorimetric assays, microfluidic networks (μ-NETs; a serpentine channel and a collection of μ-RVs separated by CBVs) and an adhesive layer. A biomedical adhesive (3M 1524) with five openings that define the sweat collection areas (19.6 mm^2) at the inlet ports provides a water-tight seal and strong bond to the skin. The microfluidic layers of PDMS consist of (1) a capping layer (thickness of ~450 μm) with a short fluid passage (blue) for measuring sweat rate and loss and (2) μ-NETs (thickness of ~700 μm) that include a serpentine microchannel for the capture/storage (volume of ~40 μl) of sweat as it emerges from the outlet of the segment of the capping layer where digital flow measurements take place (Supplementary Fig. 12) and four separate sets of connected, circular μ-RVs for chronological measurements of pH and of concentrations of sweat glucose, chloride and creatinine. Colour reference markers printed on a thin (25 μm) polyester adhesive film allow precise extraction of colour information by digital image analysis using a smartphone camera, as in previously published reports[30,31]. An illustration and a picture of the full assembled system are provided in Supplementary Fig. 13. Figure 5c shows pictures of the reference markers for each assay (left; also Supplementary Fig. 14) and images of colour development in each μ-RV for samples of artificial sweat with pH levels and chloride, creatinine and glucose concentrations within physiologically relevant ranges (right). On-body trials with healthy volunteers demonstrate measurements of sweat chloride, creatinine, glucose and pH levels using these platforms, across regions of the body with different shapes and curvatures. Image analysis at three different locations from each μ-RV provides an averaged colour value that yields, after calibration to the reference markers, quantitative information for each biomarker. Supplementary Fig. 15 highlights a specific example for the measurement of chloride concentration. Supplementary Fig. 16 shows results (sweat chloride, creatinine, glucose and pH levels) from two male participants while cycling. All values are within the normal range[30,31]. Additional tests (Supplementary Fig. 17) demonstrate the capabilities for chronological sampling from a device mounted on the forehead while home training. The data show increases in the concentration of chloride and the pH level during exercise that are comparable to the results of previous studies[32,34].

Further testing during cycling and at rest demonstrates multimodal sensing of sweat rate and loss, as well as sweat chloride, glucose and pH levels. Figure 5d shows the sweat rate (f, red) and loss (Σf; Supplementary Fig. 18), measured wirelessly every 1 min, and chloride (purple), glucose (yellow) and pH (orange) on filling each μ-RV, from a device mounted on the forehead. The error bars represent the s.d. values for the measurements of sweat rate over a 1-min averaging window (grey), and of chloride, glucose and pH levels at three different locations for each assay (black). The sweat volume (Σf) reaches 11.1, 20.7 and 31.63 μl after ~10, 14 and 23 min of exercising, respectively. The concentrations of chloride are measured to be 61.7, 62.3 and 64.5 mM after ~8, 14 and 26 min of exercising, respectively. These values are within the normal range[4], and the times for filling each μ-RV (volume, 10 μl) are consistent with those obtained using the flow-sensing platform. The increase in pH during exercise is consistent with the results of previous studies[34,35], originating from the anatomy of sweat glands and their operation. The measurements of glucose concentration are 39.2 and 70.6 μM after ~14 and 23 min of exercising, respectively. Given the reported correlation between glucose concentration in blood and sweat, the increase in glucose level might be related to release of the stress hormone cortisol during intense exercise[36–39], which causes an increase in blood glucose[40] and consequently glucose in sweat[5,41,42]. Additional details concerning the results are presented in Supplementary Note 4.

A final example of the versatility of the platform is its capability for measuring skin temperature, a critical parameter that is complementary to sweat in the context of cutaneous heat loss, body heat content and central thermoregulatory control[43]. A simple extension of the device platform involves using an additional thermistor connected in a voltage divider circuit with a known resistor (Supplementary Fig. 19a) to provide an accurate means for measuring temperature. Figure 5e shows the results of manual readings of oral (T_{oral}, purple), axillary ($T_{axillary}$, pink), temporal ($T_{temporal}$, green) and skin ($T_{skin,IR}$, blue) temperatures using basal (for T_{oral} and $T_{axillary}$) and infrared (for $T_{temporal}$ and $T_{skin,IR}$) thermometers, as well as wireless measurements of sweat (T_{sweat}, black) and skin temperatures (T_{skin}, red) as a function of time (min) using the platform in Supplementary Fig. 19b (bottom), mounted on the forearm of a male participant (Supplementary Fig. 19c) while cycling and at rest. During the session labelled 'Cycle', T_{sweat} and T_{skin} steadily decrease and reach a constant value during the session labelled 'Rest'. The difference between T_{sweat} and T_{skin} (Supplementary Fig. 20a) increases steadily from 0.2 to 0.5 °C during cycling, and then decreases and reaches a constant value (0.0 °C) during 'Rest', exhibiting a strong correlation with physical activity and with $T_{axillary}$, which increases from 35.4 to 35.9 °C during cycling and decreases and reaches a constant value while resting. $T_{skin,IR}$ depends strongly on cooling effects associated with the evaporation of sweat and, as a consequence, shows large fluctuations, decreasing as evaporative cooling increases and then returning back to the baseline after exercise. T_{oral} increases and reaches a constant value (mean ± s.d. = 37.1 ± 0.2 °C) after 10 min of exercise, and $T_{temporal}$ is relatively constant (mean ± s.d. = 35.4 ± 0.5 °C). The error bars in Supplementary Fig. 20b represent the s.d. of T_{sweat} and T_{skin} measured over a 1-min averaging window. Additional tests demonstrate the capabilities for measuring sweat rate and skin temperature using the device shown in Supplementary Fig. 19b (top), mounted on the wrist during exercise (Supplementary Fig. 21).

Conclusions

We have reported soft, wireless platforms for the accurate and reproducible analysis of sweat rate and loss, as well as skin temperature. The technology exploits a flexible circuit that combines a thermal sensing module for sweat monitoring with BLE functionality for wireless data transfer. The system requires only indirect contact with sweat, thereby preserving its sensitivity, accuracy and reusability for applications in practical conditions. Our platform can provide real-time information on sweat rate and loss, without the need for visual user engagement or complex, single-use microfluidic channels.

Our approach has the potential to be used in personalized hydration strategies, with additional promise for monitoring and managing health disorders. For example, the device can be configured to activate alerts to remind users to respond appropriately to avoid heat stress and the risks of dehydration, or to provide prompts to inform rehydration protocols in working or training environments that involve high heat stress conditions or heavy personal protective equipment. Additional potential lies in the continuous monitoring of patients during normal activities to diagnose sweat-related disorders and to assess associated treatments. Scaling laws for the effects of the thermal conductivity, heat capacity and density of the sweat and the packaging materials used around the sensor component should aid in the optimization of designs for these and other applications.

For clinical applications of these devices, an improved understanding is required of the correlations between sweat-related parameters and physiological status, including variabilities among patients. In particular, monitoring sweat rate and loss in patients with hyperhidrosis and anhidrosis, before and after alcohol consumption and in cases of insensible sweating, are interesting directions for future research. Another possibility lies in determining relationships between regional and whole-body sweat rates and electrolyte concentrations. Variations exist among and within individuals, including day-to-day variabilities, in models that predict whole-body values from regional measurements[8]. Research using a wearable unit with high temporal resolution, such as the platform introduced here, could be a valuable component in future studies.

Our modular system can be integrated with various microfluidic technologies, as well as colorimetric chemical or enzymatic reagents, to provide accurate colorimetric estimates of chloride concentration, pH and biomarkers such as creatinine and glucose. Other options include microfluidic technologies for drug delivery[44–46] or devices for the measurement of the pulse wave velocity of macrovascular and microvascular blood flow near the skin surface[47], with potential for continuous, non-invasive monitoring of blood pressure[48]. In particular, integration of thermal flow sensing platforms with drug delivery systems can also serve as a basis for control over the delivery process, through real-time measurements of release rate and exact dosages. Such technology could organize doses of medication by day and time, and assist caregivers and family members in tracking a medication schedule.

Methods

Finite-element analysis. The FEA commercial software Fluent was used to study the thermal response of the device to thermal actuation. The analysis was three-dimensional and transient, accounting for heat transfer in the fluid and solid at the ambient temperature, 25 °C. The fluid in the passage was discretized by refined hexahedron elements to ensure computational accuracy, and the properties of water (specified in Fluent) used in the simulations were viscosity $\nu_F = 0.001\,kg\,m^{-3}\,s^{-1}$, thermal conductivity $k_F = 0.6\,W\,m^{-1}\,K^{-1}$ and thermal diffusivity $\alpha_F = 0.14\,mm^2\,s^{-1}$. The flow rate, which changes with time as in experiments, was specified at the inlet of the fluid passage. The initial temperature of the fluid was the same as the ambient temperature, 25 °C. As shown in Fig. 3c, the device, attached on the tissue surface, consisted of the PDMS passage, PDMS encapsulation, and electronics involving polyimide (PI) and copper. (The model did not include a Li-polymer battery because of its large distance from the actuator and sensors.) All solid components were discretized by tetrahedral elements. The relevant material properties were $k_p = 0.27\,W\,m^{-1}\,K^{-1}$ and $\alpha_p = 0.16\,mm^2\,s^{-1}$ for the PDMS passage, $k_{PI} = 0.21\,W\,m^{-1}\,K^{-1}$ and $\alpha_{PI} = 0.11\,mm^2\,s^{-1}$ for PI and $k_{Cu} = 387\,W\,m^{-1}\,K^{-1}$ and $\alpha_{Cu} = 113\,mm^2\,s^{-1}$ for copper. A constant temperature of 32 °C was imposed on the bottom surface of the device in most studies, although 25 °C and 35 °C were also imposed to study the effect of this temperature.

Fabrication of the electronics. A thin, flexible film (AP8535R, Pyralux, DuPont) of copper/PI/copper (thicknesses of 18 μm, 75 μm and 18 μm) served as a substrate. An ultraviolet laser cutter (Protolaser U4, LPKF) ablated the copper to define conductive traces, bond pads and through-hole vias, resulting in a flexible printed

circuit board (fPCB). A silver conductive paint (cat. no. Z05001, SPI Supplies) created conductive plugs between the top and bottom patterned copper layers through the vias when heated at 90 °C using a heat gun (AOYUE Int866). Soldering paste (TS391LT, Chip Quik) was used to join the various surface-mounted components, including the BLE SoC (nRF52832, Nordic Semiconductor), antenna (2450AT18A100, Johanson Technology), amplifier (INA333, Texas Instruments), reference and heater resistors (each with a width of 0.3 mm, a length of 0.6 mm and a height of 0.25 mm; RMCF0201FT, Stackpole Electronics) and sensor components (NTC, NCP03XH, Murata), onto the fPCB by heating at 180 °C. Soft silicone materials including Silbione (RTV 4420, Bluestar Silicones) and PDMS (Sylgard 184, Dow Corning) were moulded and cured at 100 °C to form a robust encapsulating structure.

Fabrication of the flow sensing module. Fabrication of the moulds began with photolithographically defined patterns of photoresist (KMPR 1010, Microchem) formed by spin casting at 2,000 r.p.m. for 30 s on silicon wafers (thickness of 1 mm), followed by baking on a hot plate at 100 °C for 5 min, exposure to ultraviolet light at a dose of 600 mJ cm^{-2}, post-exposure baking on a hot plate at 100 °C for 5 min and immersion in developer (AZ 917MIF, Integrated Micro Materials) for 7 min. Deep reactive ion etching (STS Pegasus ICP-DRIE, SPTS Technologies) formed relief structures in the silicon to depths of 125 ± 5 µm to define a flow sensing passage. A layer of polymethylmethacrylate (PMMA; 3,000 r.p.m. for 30 s, curing at 180 °C for 2 min on a hot plate) spin cast on these moulds facilitated release of the PDMS after casting and curing. Spin-casting PDMS (Sylgard 184, Dow Corning; mixing ratio of base to curing agent of 10:1) on the PMMA-coated mould at 200 r.p.m. for 30 s, followed by degassing the sample under vacuum to remove the air bubbles, then baking on a hot plate at 150 °C for 5 min, produced a solid replica of the etched features. After release from the Si mould, a mechanical punch tool defined an inlet hole. For benchtop and body testing as shown in Figs. 2 and 4, spin-coating a layer of PDMS (10:1 mixing ratio) on PMMA-coated unpatterned silicon wafer at 1,000 r.p.m., followed by baking on a hot plate at 150 °C for 3 min, yielded an ~70-µm-thick (t_{top}) flat capping layer. This capping layer was bonded to the passage structure using oxygen plasma treatment, to complete the fabrication. For on-body testing, a CO_2 laser (Universal laser system) formed the outline of a medical-grade acrylate adhesive (1524; 3M; thickness of 60 µm). The adhesive was bonded to the bottom surface of the device after ultraviolet–ozone (UVO) treatment for 4 min to achieve water-tolerant adhesion.

Measurements of current consumed by the device. A Power Profiler Kit (PPK) board (NRF6707, Nordic Semiconductor) served as a current measurement tool for the device. The PPK supplied power to the device under test and used its ADC to measure a voltage drop across a series measurement resistor. The current consumed by the device is given by I = measured voltage drop (V)/resistor value (Ω). Through an nRF52 development kit board (nRF52-DK, Nordic semiconductor), the PPK board was connected to a computer with the PPK application, which provided a real-time display of the current measurements. Measurements of the current consumed by the device allowed estimations of battery life. With use for 1 h per day with flow measurements every minute and a 20% duty cycle of heating (heat on for 12 s before each measurement), the replaceable battery (Li-polymer battery, GMB351223; 70 mAh) in Fig. 3d (bottom) has an expected lifetime of two weeks.

Flow sensing integration with a colorimetric microfluidic module. The process includes fabrication of (1) a capping layer with a short fluid passage and (2) µ-NETs (a serpentine channel and µ-RVs separated by CBVs). Spin-casting PDMS (10:1 mixing ratio) on a microchannel (width × height of 500 µm × 125 µm) mould at 400 r.p.m., followed by baking on a hot plate at 150 °C for 5 min, produced a solid replica of the etched features. After release from the Si mould, a mechanical punch tool (1 mm in diameter) defined an inlet for entry of sweat, which then flows through a passage and then to an outlet that couples to the inlet of the serpentine channel in the µ-NETs. Bonding a 70-µm-thick flat capping layer using oxygen plasma treatment completed the fabrication of the structure of the short fluid passage. A silicon wafer (thickness of 1 mm), patterned using the above-mentioned processes, served as a mould for the µ-NETs, with relief structures to depths of 600 ± 5 µm. Spin-casting PDMS (10:1) mixed with white silicone dye (Reynolds Advanced Materials) at 3 wt% on the mould at 200 r.p.m., then baking on a hot plate at 150 °C for 3 min, allowed release of a microfluidic network layer. A mechanical punch tool was then used to define five inlet holes to couple to the skin (inlets a–e in Fig. 5a). After loading each colorimetric assay in each µ-RV, spin casting a tacky layer of PDMS (50:1 mixing ratio) at 1,000 r.p.m., then baking at 150 °C for 3 min, yielded a 75-µm-thick bonding layer between the capping layer with fluid passage and µ-NETs, in a manner aligned with the interconnect hole, through gentle contact at room temperature. A transparent polyester film with adhesive on the back side (THERMLfilm SELECT 10852, FLEXcon; thickness of 25 µm) was mounted on the top of the device with colour reference graphics for each assay. Finally, the adhesive was bonded to the bottom surface of the device after UVO treatment.

Heat distribution measurement and visualization. Images collected with an infrared camera (FLIR Systems, a6255sc) revealed the spatial distributions of surface temperature. A microfluidic module formed with PDMS mixed with a thermochromic pigment (temperature-activated thermochromic bi-colour powder pigment, Atlanta Chemical Engineering) that changes in colour from black to pink above 25 °C provided an additional means to visualize the temperature distribution.

Benchtop study. The experimental set-up and wireless electronics platform for measurements with flow rates of 0, 1, 2, 3 and 4 µl min^{-1} (set using a syringe pump, NE-300, New Era) are presented in Supplementary Fig. 1. The sensors and associated electronics were mounted on the top surface of a structure that defined a passage with inlet/outlet ports sealed to polyethylene (PE) tubing (A-M Systems, 801300). A BLE SoC configured with analogue front-end circuits controlled power to the thermal actuator and transmitted the responses of the thermistors to a BLE-enabled smartphone, for real-time graphical display and storage of the time-dependent differences in temperature between upstream (TH_{UP}) and downstream (TH_{DN}) locations.

Colorimetric assay. For chloride measurements, the assay solution used 50 mg of silver chloranilate (MP Biomedicals) dispersed in 200 µl of 2% pHEMA (poly(2-hydroxyethyl methacrylate)). Spotting 2.5 µl of this solution into the µ-RVs, followed by drying in a vacuum chamber for 1 h, prepared the system for measurements. For pH measurements, a strip of commercial indicator paper (Whatman, 2614-991) served as the assay for pH measurement. The paper was cut with a razor blade into an octagonal shape to facilitate insertion into the µ-RVs. For glucose measurements, combining the glucose substrate mix and glucose assay buffer yielded the glucose substrate solution. Spotting 0.5 µl of this substrate solution onto µ-RVs and drying under vacuum in a desiccator for 1 h produced the glucose assay. Next, spotting 0.5 µl of enzyme mixed with deionized (DI) water at an adjacent location, followed by drying in a vacuum chamber for 1 h, completed the process (Glucose Colorimetric Assay Kit II, #K686, Biovision). For creatinine measurements, solutions of creatininase, creatinase and enzyme were thoroughly mixed in a 1:1:1 ratio to yield the assay. Spotting 1.25 µl of the solution into the µ-RV, followed by drying in a vacuum chamber for 1 h, then spotting 0.75 µl of the creatinine probe at an adjacent location, followed by drying in a vacuum chamber for 2 h, completed the process (Creatinine Assay Kit, Sigma-Aldrich).

Standard colour development and colour reference marker preparation. Mixing sodium chloride, D(+)-glucose and L(+)-lactic acid (Sigma-Aldrich) in DI water yielded standard test solutions. Mixing 0.2 M sodium phosphate and 0.1 M citric acid produced pH buffer solutions with pH ranging from 4.5 to 6.5 defined by a pocket ion-sensitive field-effect transistor pH meter (Model 24004, DeltaTrak). The colorimetric devices were placed on a hot plate set at ~32 °C to mimic skin/body temperatures, to receive pipetted standard solutions into the µ-RVs for colour development. The reactions proceeded for 25 min for the chloride, creatinine and glucose assays and 5 min for the pH assay. A digital SLR camera (EOS 6D, Canon) captured images of the device. Corona treatment (Electro-Technic Products) of a polyester film for 30 s allowed efficient bonding prior to printing colour reference markers with a colour laser printer (Color image CLASS MF726Cdw, Canon) to match those determined using the methods described above. After attaching this printed polyester film on the device, a smartphone camera (iPhone 11, Apple) was used to take additional images.

Human-participant trials in practical scenarios. The experimental protocols for the on-body studies were approved by the Institutional Review Board of Northwestern University (STU00208494), and all participants provided their consent prior to test. Healthy adult volunteers (age 28–40 years, male healthy individuals) performed normal stationary cycling with no additional human-participant risk, following the provided study guidelines. Cleaning the relevant body locations with an alcohol swab enhanced adhesion by removing contaminants from the skin before device application. During cycling, a smartphone camera (iPhone 11, Apple) was used to take pictures of the devices for subsequent analysis of the digital images. Non-contact infrared (Fisher Scientific), digital (Fisher Scientific) and oral (BBT-113Ai, IProven) thermometers were used to manually measure the temperatures of the different body locations.

Digital image analysis for the evaluation of sweat concentrations. The PowerPoint Eyedropper tool defined RGB values from three random points in each µ-RV and the associated reference marker in the images. Mean normalized RGB values (R for chloride, G for pH and creatinine and B for glucose) from the references and from µ-RVs determined the range of a discrete set of known concentration points and the analyte concentration by linear interpolation (Supplementary Fig. 15), respectively.

In vitro microfluidic test and bursting pressure calculation. The bursting pressure (BP) of a CBV[49] is given by

$$\mathrm{BP} = -2\sigma\left(\frac{\cos\theta_1^*}{w} + \frac{\cos\theta_A}{h}\right)$$

where σ is the surface tension of the liquid, θ_A is the critical advancing contact angle of the fluid passage, $\theta_1^* = \min(\theta_A + \beta, 180^\circ)$ and β is the diverging angle of the passage, and w and h are the width and height of the diverging section, respectively. The surface tension of water is 0.072 N m^{-1} at the ambient temperature, and the advancing contact angle of water on PDMS is 125° ± 2° (ref. [50]).

Reporting Summary. Further information on research design is available in the Nature Research Reporting Summary linked to this article.

Data availability

Supporting data are available from the corresponding author upon reasonable request. Source data are provided with this paper.

Code availability

Custom-developed firmware for BLE SoCs and Android applications (user interfaces) for use on smartphones are available from the corresponding author upon reasonable request. All requests for source code will be reviewed by the corresponding author to verify whether the request is subject to any intellectual property or confidentiality obligations.

Received: 21 April 2020; Accepted: 16 February 2021;
Published online: 29 March 2021

References

1. Baker, L. B. Sweating rate and sweat sodium concentration in athletes: a review of methodology and intra/interindividual variability. *Sports Med.* **47**, 111–128 (2017).
2. Gambhir, S. S., Ge, T. J., Vermesh, O. & Spitler, R. Toward achieving precision health. *Sci. Transl. Med.* **10**, eaao3612 (2018).
3. Bariya, M., Nyein, H. Y. Y. & Javey, A. Wearable sweat sensors. *Nat. Electron.* **1**, 160–171 (2018).
4. Sonner, Z. et al. The microfluidics of the eccrine sweat gland, including biomarker partitioning, transport and biosensing implications. *Biomicrofluidics* **9**, 031301 (2015).
5. Gao, W. et al. Fully integrated wearable sensor arrays for multiplexed in situ perspiration analysis. *Nature* **529**, 509–514 (2016).
6. Reeder, J. T. et al. Waterproof, electronics-enabled, epidermal microfluidic devices for sweat collection, biomarker analysis and thermography in aquatic settings. *Sci. Adv.* **5**, eaau6356 (2019).
7. Bandodkar, A. J. et al. Battery-free, skin-interfaced microfluidic/electronic systems for simultaneous electrochemical, colorimetric and volumetric analysis of sweat. *Sci. Adv.* **5**, eaav3294 (2019).
8. Baker, L. B., Stofan, J. R., Hamilton, A. A. & Horswill, C. A. Comparison of regional patch collection vs. whole body washdown for measuring sweat sodium and potassium loss during exercise. *J. Appl. Physiol.* **107**, 887–895 (2009).
9. Maughan, R. J. et al. Water balance and salt losses in competitive football. *Int. J. Sport Nutr. Exerc. Metab.* **17**, 583–594 (2007).
10. Williams, C. A. & Blackwell, J. Hydration status, fluid intake and electrolyte losses in youth soccer players. *Int. J. Sports Physiol. Perform.* **7**, 367–374 (2012).
11. Al-omari, M. et al. A portable optical human sweat sensor. *J. Appl. Phys.* **116**, 183102 (2014).
12. Bandodkar, A. J. & Wang, J. Non-invasive wearable electrochemical sensors: a review. *Trends Biotechnol.* **32**, 363–371 (2014).
13. Dam, V. A. T., Zevenbergen, M. A. G. & van Schaijk, R. Toward wearable patch for sweat analysis. *Sens. Actuators B Chem.* **236**, 834–838 (2016).
14. Bain, A. R., Deren, T. M. & Jay, O. Describing individual variation in local sweating during exercise in a temperate environment. *Eur. J. Appl. Physiol.* **111**, 1599–1607 (2011).
15. Patterson, M. J., Galloway, S. D. R. & Nimmo, M. A. Variations in regional sweat composition in normal human males. *Exp. Physiol.* **85**, 869–875 (2000).
16. Matzeu, G., Fay, C., Vaillant, A., Coyle, S. & Diamond, D. A wearable device for monitoring sweat rates via image analysis. *IEEE Trans. Biomed. Eng.* **63**, 1672–1680 (2016).
17. Choi, J., Ghaffari, R., Baker, L. B. & Rogers, J. A. Skin-interfaced systems for sweat collection and analytics. *Sci. Adv.* **4**, eaar3921 (2018).
18. Francis, J., Stamper, I., Heikenfeld, J. & Gomez, E. F. Digital nanoliter to milliliter flow rate sensor with in vivo demonstration for continuous sweat rate measurement. *Lab Chip* **19**, 178–185 (2019).
19. Iftekhar, A. T., Ho, J. C.-T., Mellinger, A. & Kaya, T. 3D modeling and characterization of a calorimetric flow rate sensor for sweat rate sensing applications. *J. Appl. Phys.* **121**, 094505 (2017).
20. Brueck, A., Iftekhar, T., Stannard, B. A., Yelamarthi, K. & Kaya, T. A real-time wireless sweat rate measurement system for physical activity monitoring. *Sensors* **18**, 533 (2018).
21. Farrell, P. M. et al. Guidelines for diagnosis of cystic fibrosis in newborns through older adults: Cystic Fibrosis Foundation consensus report. *J. Pediatr.* **153**, S4–S14 (2008).
22. Moyer, J., Wilson, D., Finkelshtein, I., Wong, B. & Potts, R. Correlation between sweat glucose and blood glucose in subjects with diabetes. *Diabetes Technol. Ther.* **14**, 398–402 (2012).
23. Robinson, S. & Robinson, A. H. Chemical composition of sweat. *Physiol. Rev.* **34**, 202–220 (1954).
24. Bass, D. E. & Dobalian, I. T. Ratio between true and apparent creatinine in sweat. *J. Appl. Physiol.* **5**, 555–558 (1953).
25. Al-Tamer, Y. Y., Hadi, E. A. & Al-Badrani, I. E. I. Sweat urea, uric acid and creatinine concentrations in uraemic patients. *Urol. Res.* **25**, 337–340 (1997).
26. Harvey, C. J., LeBouf, R. F. & Stefaniak, A. B. Formulation and stability of a novel artificial human sweat under conditions of storage and use. *Toxicol. In Vitro* **24**, 1790–1796 (2010).
27. Huang, C.-T., Chen, M.-L., Huang, L.-L. & Mao, I.-F. Uric acid and urea in human sweat. *Chin. J. Physiol.* **45**, 109–115 (2002).
28. Brinkman, J. E. & Sharma, S. *Physiology*, *Metabolic Alkalosis* (StatPearls Publishing, 2019).
29. Patterson, M. J., Galloway, S. D. R. & Nimmo, M. A. Effect of induced metabolic alkalosis on sweat composition in men. *Acta Physiol. Scand.* **174**, 41–46 (2002).
30. Choi, J. et al. Soft, skin-integrated multifunctional microfluidic systems for accurate colorimetric analysis of sweat biomarkers and temperature. *ACS Sens.* **4**, 379–388 (2019).
31. Zhang, Y. et al. Passive sweat collection and colorimetric analysis of biomarkers relevant to kidney disorders using a soft microfluidic system. *Lab Chip* **19**, 1545–1555 (2019).
32. Emrich, H. M. et al. Sweat composition in relation to rate of sweating in patients with cystic fibrosis of the pancreas. *Pediatr. Res.* **2**, 464–478 (1968).
33. Ohara, K. Chloride concentration in sweat; its individual, regional, seasonal and some other variations, and interrelations between them. *Jpn J. Physiol* **16**, 274–290 (1966).
34. Coyle, S. et al. Textile sensors to measure sweat pH and sweat-rate during exercise. In *Proc. 3rd International ICST Conference on Pervasive Computing Technologies for Healthcare* 1–6 https://doi.org/10.4108/ICST.PERVASIVEHEALTH2009.5957 (ICST, 2009).
35. Oncescu, V., O'Dell, D. & Erickson, D. Smartphone based health accessory for colorimetric detection of biomarkers in sweat and saliva. *Lab Chip* **13**, 3232–3238 (2013).
36. Torrente-Rodríguez, R. M. et al. Investigation of cortisol dynamics in human sweat using a graphene-based wireless mHealth system. *Matter* **2**, 921–937 (2020).
37. Marriott, B. M. *Food Components to Enhance Performance*: *An Evaluation of Potential Performance-Enhancing Food Components for Operational Rations* (National Academic Press, 1994).
38. Robson, P. J. et al. Effects of exercise intensity, duration and recovery on in vitro neutrophil function in male athletes. *Int. J. Sports Med.* **20**, 128–135 (1999).
39. Luger, A. et al. Acute hypothalamic–pituitary–adrenal responses to the stress of treadmill exercise. *New Engl. J. Med.* **316**, 1309–1315 (1987).
40. Koc, S. The acute effect of aerobic exercise on serum cortisol levels of athletes and sedentary individuals. *J. Educ. Train. Stud.* **6**, 29–36 (2018).
41. Hong, Y. J. et al. Multifunctional wearable system that integrates sweat-based sensing and vital-sign monitoring to estimate pre-/post-exercise glucose levels. *Adv. Funct. Mater.* **28**, 1805754 (2018).
42. Emaminejad, S. et al. Autonomous sweat extraction and analysis applied to cystic fibrosis and glucose monitoring using a fully integrated wearable platform. *Proc. Natl Acad. Sci. USA* **114**, 4625–4630 (2017).
43. Sessler, D. I. Temperature monitoring and perioperative thermoregulation. *Anesthesiology* **109**, 318–338 (2008).
44. Zhang, Y. et al. Battery-free, fully implantable optofluidic cuff system for wireless optogenetic and pharmacological neuromodulation of peripheral nerves. *Sci. Adv.* **5**, eaaw5296 (2019).
45. Yeung, C. et al. A 3D-printed microfluidic-enabled hollow microneedle architecture for transdermal drug delivery. *Biomicrofluidics* **13**, 064125 (2019).
46. Lopez-Ramirez, M. A. et al. Built-in active microneedle patch with enhanced autonomous drug delivery. *Adv. Mater.* **32**, 1905740 (2020).
47. Webb, R. C. et al. Epidermal devices for noninvasive, precise and continuous mapping of macrovascular and microvascular blood flow. *Sci. Adv.* **1**, e1500701 (2015).
48. Ma, Y. et al. Relation between blood pressure and pulse wave velocity for human arteries. *Proc. Natl Acad. Sci. USA* **115**, 11144–11149 (2018).
49. Cho, H., Kim, H.-Y., Kang, J. Y. & Kim, T. S. How the capillary burst microvalve works. *J. Colloid Interface Sci.* **306**, 379–385 (2007).
50. Choi, J. et al. Soft, skin-mounted microfluidic systems for measuring secretory fluidic pressures generated at the surface of the skin by eccrine sweat glands. *Lab Chip* **17**, 2572–2580 (2018).

Acknowledgements

This work made use of the NUFAB facility of Northwestern University's NUANCE Center, which has received support from the Soft and Hybrid Nanotechnology Experimental (SHyNE) Resource (NSF ECCS-1542205), the MRSEC programme (NSF DMR-1720139) at the Materials Research Center, the International Institute for Nanotechnology (IIN), the Keck Foundation and the State of Illinois, through the IIN. J.U.K. and T.K. were supported by the Brain Research Program of the National Research Foundation (NRF) funded by the Korean government (MSIT; NRF-2019M3C7A1032076). J.C. acknowledges support from the National Research Foundation of Korea (NRF) grant funded by the Korean government (MSIT; NRF-2019R1A2C1084419). J.A.R. acknowledge support from the National Institute on Aging of the National Institutes of Health (NIH R43AG067835). We thank the Querrey-Simpson Institute for Bioelectronics for support of this work.

Author contributions

K.K., J.U.K. and J.A.R. conceived the idea, designed the research, analysed data and wrote the manuscript. K.K., J.U.K. and S.R.K. performed and were involved in the manufacturing of the sensors. K.K. designed the hardware for the wireless electronics platform. K.K., K.L. and I.Y. performed software design and software validation. Y.D. and Y.H. performed thermal and mechanical modelling. J.C., H.J., C.-J.S., Y.W., L.L., T.S.C., D.W. and J.-H.K. assisted with device fabrication. K.K. and J.U.K. performed research and led the experimental works with support from H.J., Y.P., T.K., R.G. and S.L.

Competing interests

J.A.R., S.L. and R.G. are cofounders and/or employees of Epicore Biosystems, Inc., a company that pursues commercialization of microfluidic devices for wearable applications.

Additional information

Supplementary information The online version contains supplementary material available at https://doi.org/10.1038/s41928-021-00556-2.

Correspondence and requests for materials should be addressed to J.A.R.

Peer review information *Nature Electronics* thanks Tolga Kaya, Christopher Proctor and the other, anonymous, reviewer(s) for their contribution to the peer review of this work.

Reprints and permissions information is available at www.nature.com/reprints.

Publisher's note Springer Nature remains neutral with regard to jurisdictional claims in published maps and institutional affiliations.

nature research

Corresponding author(s): John A. Rogers

Last updated by author(s): Feb 3, 2021

Reporting Summary

Nature Research wishes to improve the reproducibility of the work that we publish. This form provides structure for consistency and transparency in reporting. For further information on Nature Research policies, see our Editorial Policies and the Editorial Policy Checklist.

Statistics

For all statistical analyses, confirm that the following items are present in the figure legend, table legend, main text, or Methods section.

n/a	Confirmed	
☐	☒	The exact sample size (*n*) for each experimental group/condition, given as a discrete number and unit of measurement
☐	☒	A statement on whether measurements were taken from distinct samples or whether the same sample was measured repeatedly
☒	☐	The statistical test(s) used AND whether they are one- or two-sided *Only common tests should be described solely by name; describe more complex techniques in the Methods section.*
☒	☐	A description of all covariates tested
☒	☐	A description of any assumptions or corrections, such as tests of normality and adjustment for multiple comparisons
☐	☒	A full description of the statistical parameters including central tendency (e.g. means) or other basic estimates (e.g. regression coefficient) AND variation (e.g. standard deviation) or associated estimates of uncertainty (e.g. confidence intervals)
☒	☐	For null hypothesis testing, the test statistic (e.g. *F*, *t*, *r*) with confidence intervals, effect sizes, degrees of freedom and *P* value noted *Give P values as exact values whenever suitable.*
☒	☐	For Bayesian analysis, information on the choice of priors and Markov chain Monte Carlo settings
☒	☐	For hierarchical and complex designs, identification of the appropriate level for tests and full reporting of outcomes
☒	☐	Estimates of effect sizes (e.g. Cohen's *d*, Pearson's *r*), indicating how they were calculated

Our web collection on statistics for biologists contains articles on many of the points above.

Software and code

Policy information about availability of computer code

Data collection	Custom Android Application
Data analysis	Fluent 18.2, Matlab r2017a (custom code), Excel, PowerPoint Office 365 (RGB value), Origin Pro 9.

For manuscripts utilizing custom algorithms or software that are central to the research but not yet described in published literature, software must be made available to editors and reviewers. We strongly encourage code deposition in a community repository (e.g. GitHub). See the Nature Research guidelines for submitting code & software for further information.

Data

Policy information about availability of data

All manuscripts must include a data availability statement. This statement should provide the following information, where applicable:

- Accession codes, unique identifiers, or web links for publicly available datasets
- A list of figures that have associated raw data
- A description of any restrictions on data availability

The data and custom code that support the findings and plots of this study are available from the corresponding author upon reasonable request.

Field-specific reporting

Please select the one below that is the best fit for your research. If you are not sure, read the appropriate sections before making your selection.

☒ Life sciences ☐ Behavioural & social sciences ☐ Ecological, evolutionary & environmental sciences

For a reference copy of the document with all sections, see nature.com/documents/nr-reporting-summary-flat.pdf

Life sciences study design

All studies must disclose on these points even when the disclosure is negative.

Sample size	Total 8 subjects have participated in this study. The system performs temperature measurements at a 200-Hz sampling rate and transmits an averaged value every 0.1 seconds (10 Hz) to a user interface. In order to use digital analysis (taking pictures every one minute) as a reference, the measurement period was set to 1 minute and the sample size was determined to be 600.
Data exclusions	No data were excluded from the analysis
Replication	All electronic and microfluidic devices were successfully prepared by same fabrication processes described in the manuscript.
Randomization	All tested devices were selected randomly.
Blinding	Subjects were not blinded to use of the sensors. Data from human trials were analyzed by different authors. Blinding won't influence the experimental results.

Reporting for specific materials, systems and methods

We require information from authors about some types of materials, experimental systems and methods used in many studies. Here, indicate whether each material, system or method listed is relevant to your study. If you are not sure if a list item applies to your research, read the appropriate section before selecting a response.

Materials & experimental systems

n/a	Involved in the study
☒	☐ Antibodies
☒	☐ Eukaryotic cell lines
☒	☐ Palaeontology and archaeology
☒	☐ Animals and other organisms
☐	☒ Human research participants
☒	☐ Clinical data
☒	☐ Dual use research of concern

Methods

n/a	Involved in the study
☒	☐ ChIP-seq
☒	☐ Flow cytometry
☒	☐ MRI-based neuroimaging

Human research participants

Policy information about studies involving human research participants

Population characteristics	Age: 28-40 years old. Male healthy subjects.
Recruitment	Subjects were recruited from the Northwestern University. The subjects were voluntary. There is no potential self-selection bias.
Ethics oversight	Institutional Review Board at Northwestern University

Note that full information on the approval of the study protocol must also be provided in the manuscript.